Fourier-Space Image Processing for Spherical Experiments on OMEGA

Introduction

Measurements of shell integrity are very important for understanding and quantifying the performance degradation of spherical implosions in inertial confinement fusion (ICF).[1] Such measurements are performed at the peak of compression of the implosion, when maximum density and temperature are achieved. At this time, the hot core and the inner surface of the shell produce strong x-ray emission.[1] This radiation acts to backlight the rest of the shell. Imaging this emission at x-ray energies not absorbed by the shell provides measurements of the shape of this backlighter. Spatial modulations in the image taken at x-ray energies highly absorbed by the shell depend on modulations in both the backlighter emission and the shell's areal density.

The first measurements of shell-areal-density modulations were time integrated over the duration of the peak compression phase (~300 to 400 ps).[2–4] Core images were taken with either a monochromatic pinhole-array x-ray spectrometer[2,3] or a narrow-band filtered pinhole array[4] in targets with Ti-doped layers. The modulations in the cold, or absorbing, part of the shell's areal density $\delta[\rho R](\mathbf{r})$ are related to the modulation in the logarithm of the intensity ratio of two images taken at x-ray energies above (highly absorbing by the shell) and below (weakly absorbing by the shell) the Ti K edge:

$$\delta\left[\rho R\right](\mathbf{r}) = \delta\left\{\frac{\ln\left[I_{<K}(\mathbf{r})\right]/I_{>K}(\mathbf{r})}{\left(\mu_{>K}-\mu_{<K}\right)}\right\}, \qquad (1)$$

where $I(\mathbf{r})$ is the intensity in the image, μ is the mass absorption coefficient of Ti, and subscripts $<K$ and $>K$ designate energies just above and just below the Ti K edge, respectively.

The shell opacity and core size can vary significantly during the time of the stagnation phase, therefore time-resolved measurements of shell modulations are important. In this work, images above and below the Ti K edge are captured with a framing camera and recorded on film. The imaging system, composed of the pinhole array, the framing camera, the film, and the digitization process, is fully characterized. Image processing techniques are accomplished in spatial-frequency, or Fourier, space. In the sections that follow: (1) The image formation at all four stages of the imaging system is described along with approximations that enable the modulations in captured images to be related to shell-areal-density nonuniformities. (2) The pinhole camera and framing camera resolution are described. (3) The most important sources of experimental noise are investigated: the statistical x-ray photon noise from the core emission, the framing camera noise, the film noise, and the digitization noise. Methods of noise reduction are discussed. (4) A noise filtering and resolution deconvolution method based on Wiener filtering is formulated, and the experimental uncertainties along with the approximations are discussed. Conclusions are presented in the final section.

Experimental Configuration

The shell-areal-density modulation has been measured for shot 19669 in which a spherical target with an initial diameter of 921 μm, a 19.8-μm-thick shell, and 15-atm-D_2 fill was imploded by 351-nm laser light using the 60-beam OMEGA laser system.[5] A 1-ns square pulse shape with total on-target energy of about 23 kJ was used in this experiment. The target shell had a 2.4-μm-thick, Ti-doped (7.4% by atom) CH layer, which was separated from the inner surface by a 1.1-μm-thick pure-CH layer. The 15.3-μm outer layer was pure CH. Beam-smoothing techniques used during these experiments included distributed phase plates (DPP's)[6] and 0.2-THz smoothing by spectral dispersion (SSD).[7]

The target emission during the peak of compression was imaged by a 6-μm pinhole array (protected by a 203.2-μm Be filter) on a framing camera. The upper two strips of the framing camera were filtered by a 75-μm-thick Ti filter and the lower two strips by a 50-μm-thick Fe filter to image core radiation above (~6.5 keV) and below (~4.9 keV) the Ti K edge, simultaneously. The spectral bandwidth of these two x-ray energy channels was about $\Delta E/E \approx 0.2$ and similar to the time-

integrated measurements.[4] The distance between the target and the pinhole array was 3 cm, and the distance between the pinhole array and the framing camera was 36 cm, resulting in a magnification of 12 (Fig. 84.33). Each image taken with a framing camera had a temporal resolution of ~40 ps.[8] The use of optical fiducial pulses coupled with an electronic monitor of the framing camera produced a frame-timing precision of ~70 ps. The framing-camera output was captured on Kodak T-Max 3200 film, which was then digitized with a Perkin-Elmer microdensitometer (PDS) equipped with a 20-μm-square scanning aperture.

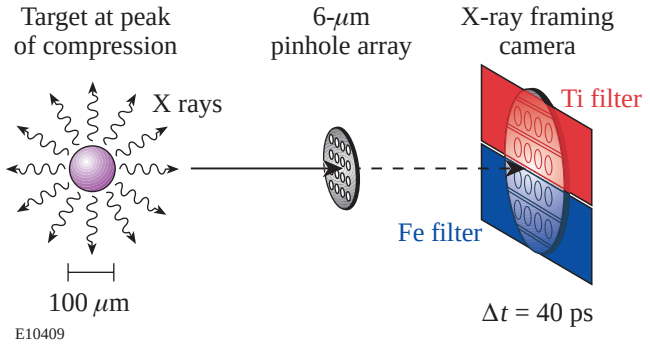

Figure 84.33
Schematic of the framing camera.

Figure 84.34 shows "raw" core images at the peak of compression below [(a), (b)] and above [(c), (d)] the Ti *K* edge, taken at 2.25 ns [(a), (c)] and at 2.30 ns [(b), (d)]. Notice that the two images within a particular energy channel have similar features that are different from the features in the other energy channel. This indicates that the features seen in the images are not noise and that the difference between the images at different energies is due to modulations in the absorbing shell. The main purpose of this article is to characterize the resolution and noise of all parts of the imaging system in order to distinguish signal from noise and relate detected modulations in the images to modulations in the shell. Figure 84.35 shows a block diagram of the entire detection system, which comprises four major parts: the 6-μm pinhole, the framing camera with a microchannel plate (MCP) and a phosphor plate, the film, and the digitization process. At each stage of the measurement, noise is added to the signal, and the signal with noise is convolved with the point-spread function (PSF) of each component of the system. In the spatial-frequency domain, the spectra of both the signal and the noise are multiplied by a modulation transfer function (MTF, defined here as the Fourier transform of the PSF) of that component of the imaging system.

The x-ray intensity leaving the target at time t and energy E is defined as

$$I_0(E,\mathbf{r},t) = I^{\text{core}}(E,\mathbf{r},t)\,\exp\left[-D_0(\mathbf{r},t)\right], \tag{2}$$

where $\mathbf{r}$ is the spatial coordinate, I_{core} $(E,\mathbf{r},t)$ is the core emission intensity integrated over the core size in the direction of light propagation from the target to the detector, and $D_0(E,\mathbf{r},t) = \mu(E)[\rho R](\mathbf{r},t)$ is the optical depth of the Ti in the shell. The absorption in CH is negligible compared to Ti in this experiment at an energy range from 5 to 7 keV.[4] The light intensity leaving the framing camera and incident on the film is

$$\begin{aligned} & I_{i2}(\mathbf{r},t) \\ & \sim \int dE \int d\mathbf{r}' R_{1,2}(E,\mathbf{r}-\mathbf{r}',t)\; f_1(E)\,\mu_{\text{Au}}(E)\,I_{i0}(E,\mathbf{r}',t) \\ & + I_{i\text{back}}(\mathbf{r},t), \end{aligned} \tag{3}$$

where the subscript i ($i = a$ or b) corresponds to images taken above and below the Ti *K* edge, respectively, $R_{1,2}(E,\mathbf{r},t)$ is the

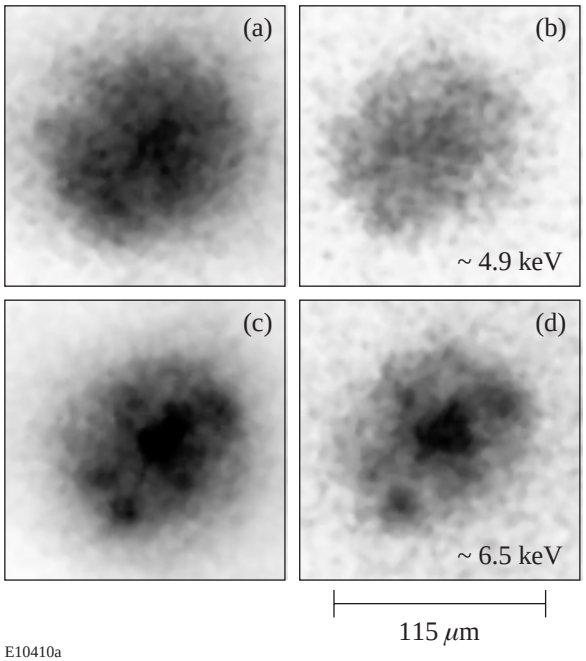

Figure 84.34
"Raw" core images at the peak of compression below [(a), (b)] and above [(c), (d)] the Ti *K* edge, taken at 2.25 ns [(a), (c)] and 2.30 ns [(b), (d)].

PSF of the pinhole and framing cameras that is in general a function of the x-ray energy E, $f_i(E)$ is the filter function of the ith energy channel, $\mu_{Au}(E)$ is the mass absorption rate of the gold photocathode (in the MCP), and $I_{i\text{back}}(E,\mathbf{r},t)$ is the background intensity for the ith channel. The background intensity is normally slowly varying and comes from hard x rays penetrating directly through the 25-μm-thick Ta substrate in which the pinholes are contained.

The film converts the incident light intensity $I_{i2}(\mathbf{r},t)$ into the film optical density O_{i3} $(\mathbf{r},t)$ according to its sensitivity [or D log(H)] curve W. Convolved with the PSF of the film $R_3(\mathbf{r},t)$, $O_{i3}(\mathbf{r},t)$ is given by

$$O_{i3}(\mathbf{r},t) = \int d\mathbf{r}' R_3(\mathbf{r}-\mathbf{r}')\, W\left\{\log_{10}\left[\int_{t-\tau/2}^{t+\tau/2} dt' I_{i2}(\mathbf{r}',t')\right]\right\}, \quad (4)$$

where τ = 40 ps is the temporal resolution of the framing camera. During film digitization, the optical density $O_{i3}(\mathbf{r},t)$ is convolved with the PSF $R_4(\mathbf{r})$ of the 20-μm-square aperture in the PDS to give the digitized or measured optical density

$$O_{i4}(\mathbf{r},t) = \int d\mathbf{r}' R_4(\mathbf{r}-\mathbf{r}') O_{i3}(\mathbf{r}',t). \quad (5)$$

The optical density of the film, $O_{i4}(\mathbf{r},t)$, is converted to intensity using the inverse film sensitivity W^{-1}; simultaneously the flat background intensity $I_{i\text{back}}(\mathbf{r},t)$ can be subtracted from the image because the constant $I_{i\text{back}}(\mathbf{r},t)$ is not affected by the convolutions in Eqs. (4) and (5). The measured optical depth $D_{i5}(\mathbf{r},t)$ of the target at a particular energy channel is obtained by taking the natural logarithm of that intensity-converted image,

$$D_{i5}(\mathbf{r},t) = \ln\left\{10^{W^{-1}[O_{i4}(\mathbf{r},t)]} - I_{i\,\text{back}}(\mathbf{r},t)\right\}. \quad (6)$$

Measured shell modulations $d_5(\mathbf{r},t)$ in optical depth are the differences in modulation optical depth of images above and below the Ti K edge,

$$d_5(\mathbf{r},t) = \delta\left[D_{a5}(\mathbf{r},t) - D_{b5}(\mathbf{r},t)\right]. \quad (7)$$

The blue line in Fig. 84.36 shows the measured shell modulation spectrum as a function of spatial frequency. This spectrum was obtained by azimuthally averaging the Fourier amplitude of the measured optical-depth-difference images above $[D_{a5}(\mathbf{r},t)]$ and below $[D_{b5}(\mathbf{r},t)]$ the Ti K edge. Each image was obtained by averaging two images below the K edge [shown in Figs. 84.34(a) and 84.34(b)] $D_{b5}(\mathbf{r},t) = [D_{b5}(\mathbf{r},t_1) + D_{b5}(\mathbf{r},t_2)]/2$, and two images above the K edge [shown in Figs. 84.34(c) and 84.34(d)] $D_{a5}(\mathbf{r},t) = [D_{a5}(\mathbf{r},t_1) + D_{a5}(\mathbf{r},t_2)]/2$. The noise level, shown by a red line in Fig. 84.36, was obtained by analyzing in Fourier space the differences in the two images above $[N_{a5}(\mathbf{r},t)]$ and below $[N_{b5}(\mathbf{r},t)]$ the K edge, respectively. It was assumed that there was little difference between images taken 50 ps apart. The black line represents the film noise, which was obtained by analyzing the same-size area as in the above images (1.4 mm × 1.4 mm) of uniformly exposed (optical density ~1) film.

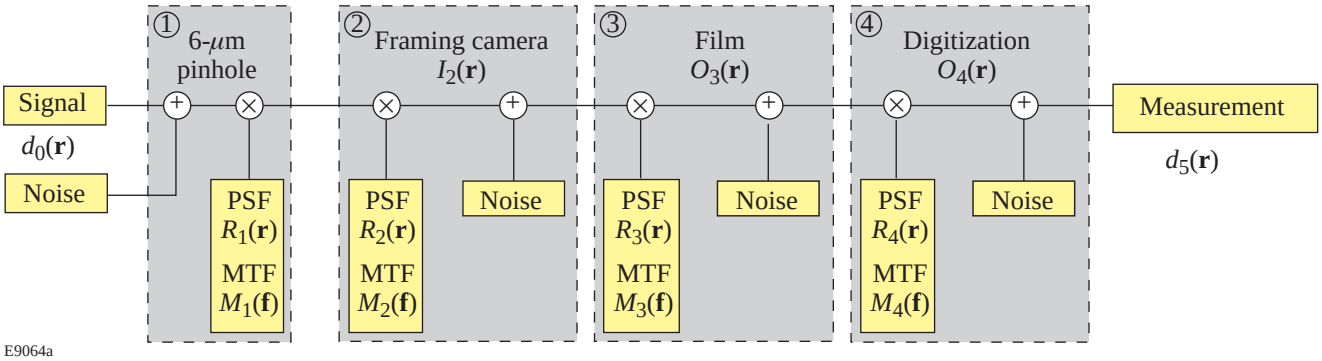

Figure 84.35
Block diagram of the experimental detection system, which comprises four major parts: a 6-μm pinhole, the framing camera, the film, and the digitization. At each stage of measurement, noise is added to the signal, and the signal with noise is convolved with the PSF. Variables $d_0^{sh}(\mathbf{r},t)$ and $d_5(\mathbf{r},t)$ are the optical-depth modulations in the shell and measured on a film, respectively. $I_2(\mathbf{r},t)$ is the light intensity in the framing camera's output. $O_3(\mathbf{r},t)$ and $O_4(\mathbf{r},t)$ are the optical density of the film, before and after digitization, respectively.

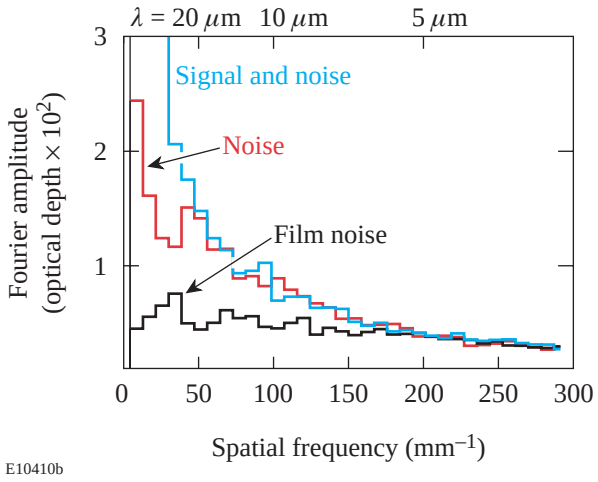

Figure 84.36
Azimuthally averaged Fourier amplitude as a function of spatial frequency for the signal with noise (blue line), the noise (red line) of the measured optical-depth modulations from the images in Fig. 84.34, and the film noise (black line).

One advantage of performing noise analysis in spatial-frequency space is the possibility of determining the origin of the noise from the shape of the noise spectrum. At each stage of the imaging system, the spectra of both the signal and the noise are multiplied by the MTF of that particular part of the system. Therefore, an initially flat noise spectrum—for example, the statistical x-ray photon noise from the core emission—will follow the shape of the pinhole camera's MTF after being imaged by the pinhole camera. Figure 84.36 shows that the film noise dominates at high spatial frequencies (>200 mm^{-1}), which slowly falls as a function of spatial frequency following the MTF of the 20-μm-square scanning aperture. At lower spatial frequencies (<200 mm^{-1}), the noise falls more steeply and, as will be shown later, is dominated by photon statistics from the core emission in this spectral region.

To recover the target optical depth $D_0(E,\mathbf{r},t)$ from the measured optical depth $d_5(\mathbf{r},t)$ it is, in general, necessary to work backward through all four stages of the imaging system, compensating for noise and system response (PSF). Additional complications arise during signal conversions from optical density to intensity and finally to the shell's optical depth. These conversions are nonlinear [see Eqs. (2), (4), and (6)]; therefore, additional noise is generated from the coupling of signal and noise during each conversion. However, if the modulations in the target's optical depth are small (which is the case in our experiment), the entire imaging system may be considered linear. This greatly simplifies the relation between the measured and target optical depths and enables a direct linear relationship between them. This method is justified when all of the nonlinear effects are small and may not be detected within system noise.

If the shell's optical-depth modulations are small for the energy channels above and below the Ti K edge, the core intensity consists of the smooth envelope and small modulations and has the same spatial and temporal structure for both the above- and below-K-edge energy channels, then can be summarized as

$$D_{i0}^{\mathrm{sh}}(\mathbf{r},t) = D_i^{\mathrm{sh}}(t) + d_{i0}^{\mathrm{sh}}(\mathbf{r},t), \tag{8}$$

$$I^{\mathrm{core}}(\mathbf{r},t) \sim I^{\mathrm{env}}(\mathbf{r},t)\,\exp\left[-d_0^{\mathrm{core}}(\mathbf{r},t)\right], \tag{9}$$

where $D_{i0}^{\mathrm{sh}}(\mathbf{r},t)$ is the total shell optical depth;

$$d_{i0}^{\mathrm{sh}}(\mathbf{r},t) = \mu_i \delta[\rho R](\mathbf{r},t) < 1$$

and $d_0^{\mathrm{core}}(\mathbf{r},t) < 1$ are the optical-depth modulations of the shell and the core, respectively; $I^{\mathrm{env}}(\mathbf{r},t)$ is the slowly varying envelope of the core emission; and μ_i is the spectrally weighed mass absorption rate of cold Ti at a particular energy channel [it is determined by the filter function $f_i(E)$ and core emission spectrum $I^{\mathrm{core}}(E,\mathbf{r},t)$]. The modulation in the shell's optical depth is simply the difference in optical-depth modulations above and below the K edge:

$$d_0^{\mathrm{sh}}(\mathbf{r},t) = d_{a0}^{\mathrm{sh}}(\mathbf{r},t) - d_{b0}^{\mathrm{sh}}(\mathbf{r},t). \tag{10}$$

Since the shell and core modulations are small, it is possible to expand the exponential functions in Eqs. (2) and (9) into Taylor series; retaining only zeroth and first orders in these expansions, we have the following expression for Eq. (3):

$$I_{i2}(\mathbf{r},t) \sim I^{\mathrm{env}}(\mathbf{r},t)\left\{2C - \left[\int d\mathbf{r}' R_{1,2}(\mathbf{r}-\mathbf{r}',t)\, d_{i0}^{\mathrm{sh}}(\mathbf{r}',t)\right.\right.$$

$$\left.\left. + \int d\mathbf{r}' R_{1,2}(\mathbf{r}-\mathbf{r}',t)\, d_0^{\mathrm{core}}(\mathbf{r}',t)\right]\right\}, \tag{11}$$

where $C = \int d\mathbf{r} R_{1,2}(\mathbf{r},t)$ is a normalization constant and the background intensity is assumed to be zero, $I_{i\mathrm{back}}(\mathbf{r},t) = 0$. T-MAX 3200 film has a constant MTF at least up to a spatial frequency of ~50 mm^{-1}, the highest spatial frequency considered in the experiment, so the PSF of the film is set to the delta function $\delta(\mathbf{r})$. Since only the "linear" part of the film sensitivity [D log(H)] curve is used, the modulations in measured optical

depth are linearly related to the optical-depth modulations in the target:

$$d_{i5}(\mathbf{r},t) = \int d\mathbf{r}' R_{\rm sys}(\mathbf{r}-\mathbf{r}',t)\, d_0^{\rm sh}(\mathbf{r}',t) + \int d\mathbf{r}' R_{\rm sys}(\mathbf{r}-\mathbf{r}',t)\, d_0^{\rm core}(\mathbf{r},t), \quad (12)$$

where $R_{\rm sys}(\mathbf{r},t)$ is the PSF of the entire system. It is normalized, $\int d\mathbf{r} R_{\rm sys}(\mathbf{r},t) = 1$, and proportional to the convolution of PSF's of the pinhole camera, the framing camera, and the digitizing aperture of the densitometer. In frequency space, the system MTF is the product of the MTF's of each of these components. Equation (12) was obtained by substituting Eq. (11) into Eqs. (4)–(6) and retaining only the zeroth-order and first-order terms of the Taylor series expansion of the logarithm function. Subtracting the optical-depth images above and below the *K* edge, the measured modulation in the cold-shell optical depth is given by

$$d_5(\mathbf{r},t) = d_{a5}(\mathbf{r},t) - d_{b5}(\mathbf{r},t) = \int d\mathbf{r}' R_{\rm sys}(\mathbf{r}-\mathbf{r}',t)\, d_0^{\rm sh}(\mathbf{r}',t). \quad (13)$$

The measured optical-depth modulations calculated from images above and below the Ti *K* edge are linearly related to the shell optical-depth modulations if these modulations are small. As mentioned earlier in this section, the core intensity $I^{\rm core}(\mathbf{r},t)$ has the same spatial and temporal structure for both the above- and below-*K*-edge energy channels. This assumption was experimentally confirmed in time-integrated experiments with pure-CH shells[4] and was used to derive Eq. (13) for time-resolved imaging.

In summary, approximations of the system performance have been used to find a straightforward relationship between the measured optical-depth modulations and the cold-shell areal-density modulations. Equation (13) has been derived by assuming that the shell's optical-depth modulations are small compared to unity. Since Eq. (13) is a linear approximation, it does not treat the generation of harmonics and coupling of modes produced by system nonlinearities. These nonlinearities have been simulated for amplitudes of modulations similar to that in data shown in Fig. 84.34, and the nonlinear effects were found to be negligible compared to the system noise.

System Resolution

The system resolution is determined from the point-spread function (PSF) in real space or the modulation transfer function (MTF) in spatial-frequency space, which is defined in this article as the Fourier transform of the PSF. The system MTF is the product of the MTF's of each of these components: the pinhole camera, the 20-μm-square scanning aperture, and the framing camera. The first two are determined from calculations based on geometry and spectral energy.

The digitizing PSF is proportional to Δx = 20-μm-square aperture; therefore, the MTF, which is the Fourier transform of the aperture, is given by[9]

$$M_{\rm dig}(f_x, f_y) = \left[\frac{\sin(\pi \Delta x\, f_x)}{\pi \Delta x\, f_x}\right]\left[\frac{\sin(\pi \Delta x\, f_y)}{\pi \Delta x\, f_y}\right], \quad (14)$$

where f_x, f_y are the spatial-frequency components of the vector **f**.

The MTF of the framing camera was determined by measuring the camera response to an edge placed ~1 mm in front of the camera and backlit by x rays. This output of the framing camera was measured with a charge-coupled-device (CCD) camera[10] with 9-μm-square pixel size. The edge was close enough to the framing camera so that diffraction effects can be neglected. The dashed line in Fig. 84.37(a) represents the light intensity incident on the edge. The blue line is the measured light intensity propagated through the system (and averaged in the direction parallel to the edge), and the red line is the fit to experimental data assuming the framing camera MTF as a two-Gaussian function,[11]

$$M_{\rm fc}(f) = \alpha_1 \exp\left[-(\sigma_1 f)^2\right] + \alpha_2 \exp\left[-(\sigma_2 f)^2\right], \quad (15)$$

where $\alpha_1 = 0.89 \pm 0.01$, $\alpha_2 = 0.22 \pm 0.01$, $\sigma_1 = 105.4 \pm 0.4\ \mu$m, and σ_2 = 2356.8±0.4 μm. The measured MTF of the framing camera is shown in Fig. 84.37(b). This MTF is similar to that measured in the earlier experiments.[12] The only difference is that CCD measurements are more sensitive than film measurements, and it was possible to detect the long-scale-length scattering of photons and electrons between the phosphor and microchannel plates.[13] This scatter is given by the second term in Eq. (15), and it reduces the MCP resolution by about 10% at low spatial frequencies <5 mm^{-1}.

The resolution of the pinhole camera was calculated using the Fresnel approximation (which should work well for the parameters of our imaging system) for the light propagation.[9] The pinhole PSF is given by the following equation:[9]

$$P_{\mathrm{ph}}(x,y,z_2) \sim \frac{1}{\left(\lambda^4 z_1^2 z_2^2\right)} \cdot \left| \iint dx'dy' \mathrm{circ}\left(\frac{x',y'}{d}\right) \exp\left[-\frac{i\pi}{\lambda}\left(x'^2+y'^2\right)\left(\frac{1}{z_1}+\frac{1}{z_2}\right)\right] \exp\left[\frac{2i\pi}{(\lambda z_2)}(xx'+yy')\right]\right|^2, \quad (16)$$

where circ($x,y/d$) is the circular aperture function with diameter d, λ is the x-ray wavelength, and z_1, z_2 are the distances from the object to the pinhole and the pinhole to the image, respectively. Because the pinhole size d in the pinhole array was varying typically within a specification of 0.5 μm, d = 6±0.5 μm, it was important that the pinhole-size variation not affect the pinhole resolution. Figure 84.38(a) shows the calculated pinhole MTF's of 5-, 6-, and 7-μm-diam pinholes at an x-ray energy of 5 keV. Even though the MTF's are different at high spatial frequencies, there is little difference (<5%) for all three MTF's at low spatial frequencies (<50 mm^{-1}), where all detected above the noise signal are located (see Fig. 84.36). Figure 84.38(b) shows that calculated MTF's of 6-μm pinholes at 5 and 7 keV are very close (with differences also <5%) at low spatial frequencies (<50 mm^{-1}). The pinhole depth's effect on the resolution was found to be negligible for the experimental conditions. This confirms the assumption made in the previous section that the system resolution is the same for images above and below the K edge.

System Noise

To determine the origin of noise shown by the black line in Fig. 84.36, the noise of the entire imaging system and in its individual parts was characterized by Fourier space analysis of uniformly exposed areas with the same box size (1.4 mm × 1.4 mm in image plane) as the data in Fig. 84.36. To measure noise in the entire system, images of a large area (~1 mm in diameter) of a uranium backlighter were used. The backlighter target was illuminated by 12 overlapping beams at an intensity of ~10^{14} W/cm^2, in a configuration similar to the noise measurements for planar-foil experiments.[12] Since the backlighter

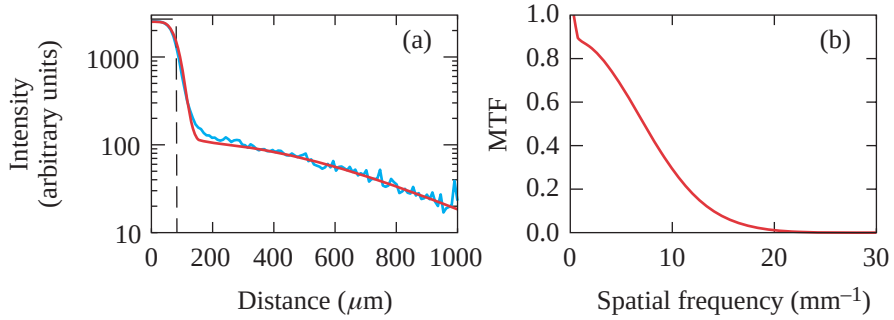

Figure 84.37
The framing camera resolution. The blue line in (a) represents the light intensity incident on the edge. The red line is the measured light intensity propagated through the system (and averaged in the direction parallel to the edge). The red line is the fit to experimental data assuming the framing camera MTF shown in (b).

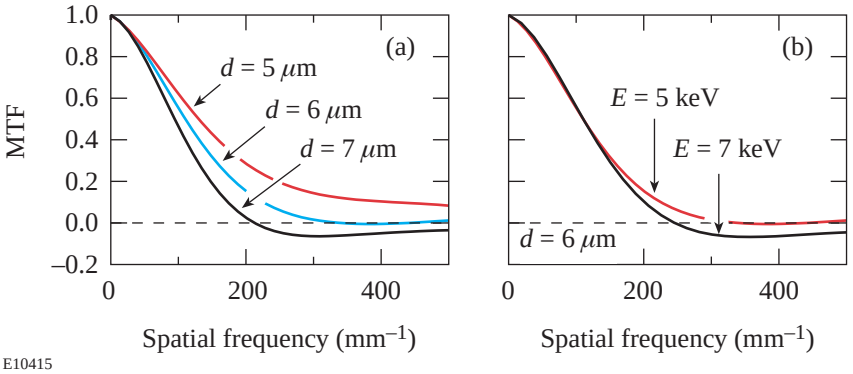

Figure 84.38
The resolution of the pinhole camera. (a) The calculated pinhole MTF's of 5-, 6-, and 7-μm-diam pinholes at an x-ray energy of 5 keV. (b) The calculated 6-μm pinhole MTF's at x-ray energies of 5 and 7 keV.

emission was smooth, the nonuniformities in the images were considered to be caused by noise. A 25-μm "strip" of CH_2 was placed between the backlighter and the pinhole to attenuate the backlighter emission by a factor of ~8 at 1.3 keV (see Fig. 84.39). The filters in front of the framing camera were also varied to change the exposure levels by a predetermined amount.

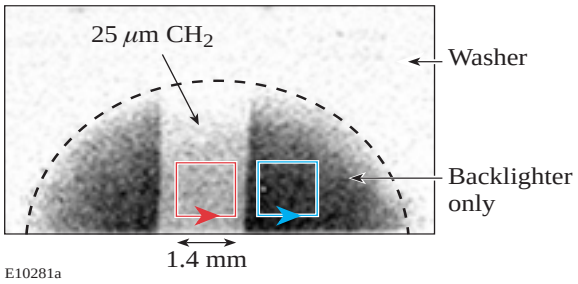

Figure 84.39
The image of the 25-μm CH_2 "strip" target taken with a U backlighter. Two boxes in the strip and backlighter-only regions represent image areas taken for analysis.

Figure 84.40 shows the azimuthally averaged Fourier amplitudes of the optical depth for two square regions with 1.4 mm in image plane, through (blue lines) and around (red lines) the strip. The total filtration in front of the framing camera included 20 μm of Be and 12 μm of Al for the data shown in Fig. 84.40(a) and 9 μm of Al for the data in Fig. 84.40(b). As a result of the filters, a relatively narrow band ($\Delta E/E \approx 0.2$) of x rays around 1.3 keV is used for radiography. At high spatial frequencies ($f > 200$ mm^{-1}), the noise spectrum is nearly constant, indicative of the noise from film and digitization. At lower spatial frequencies the noise amplitudes depend on the MTF's of pinhole and framing cameras and have contributions from both the photon statistical noise of the backlighter x rays and framing camera noise. It will be shown later in this section that the amplitude of framing camera noise is proportional to the output intensity. This means that in optical-depth space the framing camera noise is independent of the intensity (because the optical depth is the logarithm of the intensity), and it is expected to be the same in the areas through and around the strip. In optical-depth space, the photon noise of backlighter x rays is inversely proportional to the square root of the number of photons.[12] There is more photon noise in the region of the strip with fewer x-ray photons than in the region out of the strip [shown in Fig. 84.40(a)]. The noise falls even more with decreasing amount of filtration reaching the film noise level. This indicates that photon noise is dominant in the low-spatial-frequency region of the data shown in Figs. 84.36 and 84.40.

Figure 84.41 shows spectra of digitizing noise and the film noise in optical density versus spatial frequency. The digitizing noise [Fig. 84.41(a)] has been measured by digitizing uniform light exposures (with no film) using six different filters with transmissions of 0.5, 1.1, 1.5, 1.9, 2.4, and 2.9 optical density. To measure the film noise, the film was exposed to uniform irradiation at five different exposure levels of 0.5, 1.1, 1.7, 2.9, and 3.8 optical density [Fig. 84.41(b)]. A 5-μm-square digitizing aperture was used, and the analysis box size was the same as for all other images in this article: 1.4 mm square in image plane. The digitizing noise spectra are flat functions of spatial frequency, as expected, because the digitizing noise is added to the measurement after the effect of the system resolution. The noise amplitudes increase at higher optical-density levels when light transmission through the filter decreases. The film noise, which is about ten times higher than the digitizing noise (as evident from Fig. 84.41), also depends weakly on the exposure level. At high spatial frequencies its amplitude decreases gradually, as expected, since they are multiplied by the 5-μm-square digitizing aperture MTF given by Eq. (14).

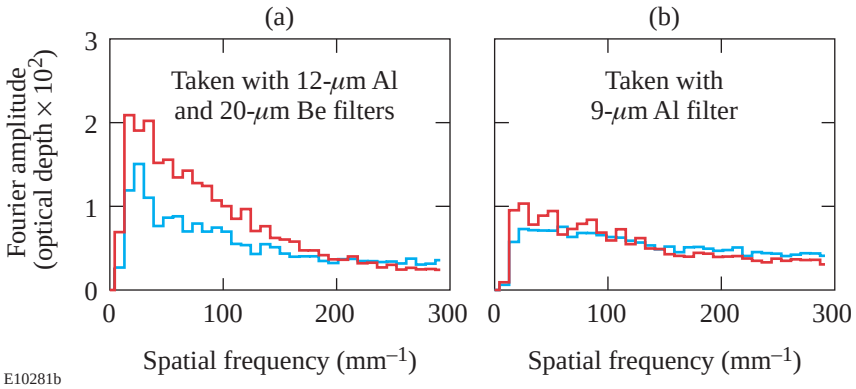

Figure 84.40
System noise. The measured noise spectra in areas through (blue lines) and around (red lines) the 25-μm-CH_2 strip target taken with (a) 20-μm-Be and 12-μm-Al filters, and (b) a 9-μm-Al filter.

Framing camera noise could be measured once the film was replaced by the CCD camera,[10] which allowed lower noise amplitudes to be detected. Figure 84.42(a) shows noise spectra of framing camera outputs taken with film and with the CCD. The framing camera was uniformly illuminated by x rays during two similar flat-field exposures (one exposure was taken with film, the other with a CCD). The incident x-ray flux was kept high to minimize the photon noise of incident x rays. The film exposure was converted to intensity in order to compare it with CCD data, which measures intensity, not optical density. Film data were digitized with a 10-μm-square digitizing aperture; the CCD's pixels were 9 μm. Film noise dominates framing camera noise at high spatial frequencies, and both noise levels are comparable at low spatial frequencies. The spectral shape of the framing camera noise follows the MTF (shown in Fig. 84.37).

Figure 84.42(b) shows the dependence of the framing camera noise on output intensity. By varying the gain of the framing camera, three different areas (with a typical square box of 1.4 mm) had average exposure levels of 200, 650, and 3600 counts measured with the CCD during one of the flat-field exposures. The noise spectra corresponding to these data are shown by three lines in Fig. 84.42(b). The noise levels scale as the average exposure levels on the CCD, indicating that the framing camera noise is proportional to the output intensity. This noise is dominated by the gain variations inside the MCP, which are reproducible from shot to shot. Figure 84.43 shows two images of the same area of the framing camera outputs taken during two different flat-field exposures. Images are virtually identical. Since this noise is reproducible, it can be removed from the images by subtracting two images. In Fig. 84.44 the noise spectra of these two images is shown by red and black lines. The blue line represents the noise from the difference of two images. The framing camera noise is reduced by a factor of 4 at low spatial frequencies. Such noise reduction can be useful in image processing when the framing camera noise is dominant (with the CCD).

In summary, the photon statistics of x rays are the dominant source of noise in our measurements. By increasing the inci-

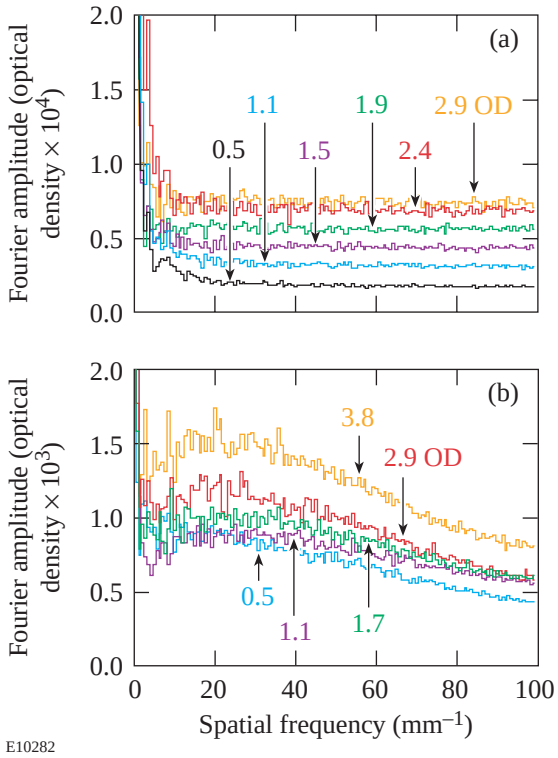

Figure 84.41
Fourier spectra of digitizing and film noise versus spatial frequency. (a) The digitizing noise measured by digitizing uniform light exposures (with no film) using six different filters with transmissions of 0.5, 1.1, 1.5, 1.9, 2.4, and 2.9 optical density. (b) The film noise measured by digitizing uniform film exposures at five different exposure levels of 0.5, 1.1, 1.7, 2.9, and 3.8 optical density.

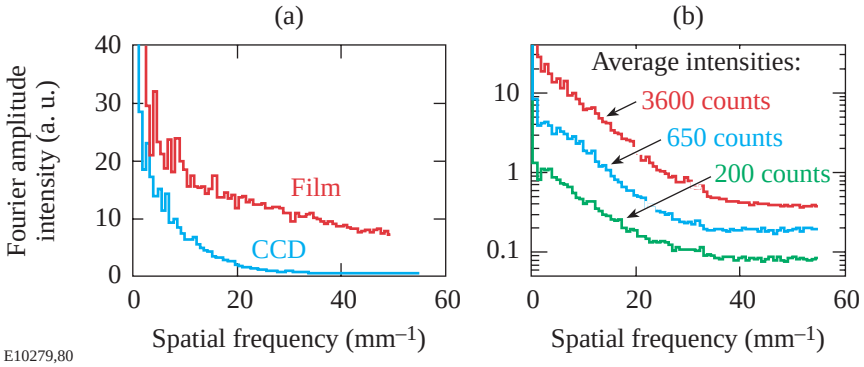

Figure 84.42
The framing camera noise. (a) The comparison of framing camera noise spectra taken with film and with a CCD. (b) The framing camera noise at different output intensities of 200, 650, and 3600 counts taken during a flat-field exposure with a CCD.

dent photon flux it was possible to reduce the noise to the levels where the framing camera and film noise became important. In this situation, an additional noise reduction was possible when the film was replaced by the CCD camera, and the framing camera noise was reduced by removing the shot-to-shot repeatable structure in the framing camera output.

Wiener Filtering

Using the measured system resolution and noise, it is possible not only to distinguish signal from noise in Fig. 84.36 but also to reduce it and deconvolve the resolution from the data detected above the noise. Such image processing is possible with Wiener filtering in spatial-frequency space. If $C(\mathbf{f})$ is the signal plus noise measured by the system (blue line in Fig. 84.36), $C(\mathbf{f}) = S(\mathbf{f}) + N(\mathbf{f})$, then the restored signal $R(\mathbf{f})$ is[14]

$$R(\mathbf{f}) = \frac{C(\mathbf{f})}{M_{\text{sys}}(\mathbf{f})} \bullet \frac{\left|S(\mathbf{f})\right|^2}{\left|S(\mathbf{f})\right|^2 + \left|N_{\text{avg}}(\mathbf{f})\right|^2}, \tag{17}$$

where $M_{\text{sys}}(\mathbf{f})$ is total system MTF, which is the product of the 6-μm pinhole camera MTF (Fig. 84.38), the framing camera MTF [Fig. 84.37(b) and Eq. (15)], and the 20-μm-square digitizing aperture MTF [Eq. (14)]. The last two MTF's are applied assuming a system magnification of 12. The term $\left|N_{\text{avg}}(\mathbf{f})\right|$ is the average noise spectrum (the black line in Fig. 84.36). During Wiener filtering the amplitudes that have $\left|C(\mathbf{f})\right| < 1.5\left|N_{\text{avg}}(\mathbf{f})\right|$ plus all amplitudes with spatial frequencies >50 mm^{-1} (this corresponds to wavelengths shorter than 20 μm) were filtered because the noise is dominant there. For the rest of the spectrum, it was assumed that the unknown variable $S(\mathbf{f})$ can be obtained by subtracting the noise in quadrature from the measured signal plus noise, $\left|S(\mathbf{f})\right|^2 = \left|C(\mathbf{f})\right|^2 - \left|N_{\text{avg}}(\mathbf{f})\right|^2$.

Figure 84.45 shows the result of such image processing, the image of the shell's optical-depth modulations. The level of shell modulations is similar to the time-integrated measurements,[4] which have detected ~20% perturbations in cold-shell areal density. The errors in determining these modulations, besides the system noise, include the uncertainty in the system

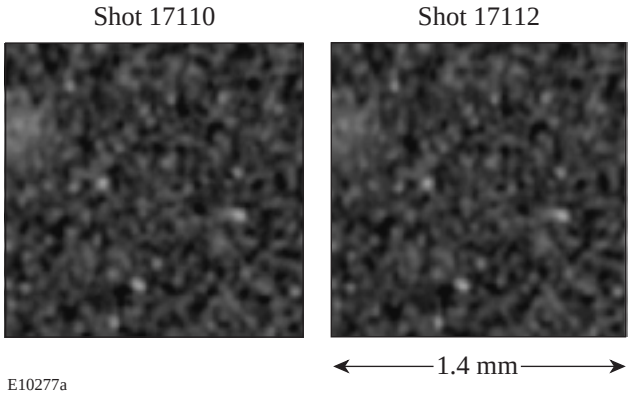

Figure 84.43
Two images of the same area of the framing camera outputs taken during two different flat-field exposures with a CCD. The images are nearly identical.

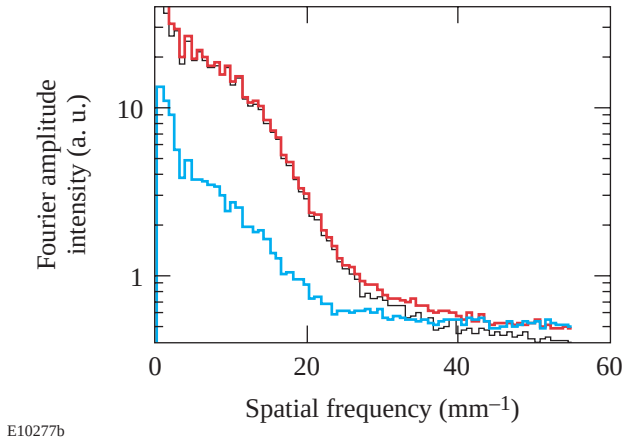

Figure 84.44
Reduction of the framing camera noise. The noise spectra of two images from Fig. 84.43 shown by red and black lines. The blue line represents noise from the difference of two images showing that framing camera noise can be reduced by a factor of 4 at low spatial frequencies.

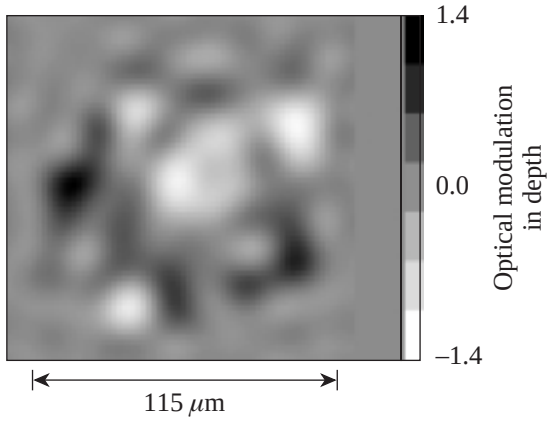

Figure 84.45
The Wiener-filtered image of the shell's optical-depth modulations.

MTF (which was about 5%) and the uncertainty in linearization of the nonlinear imaging system. This error was estimated by calculating the deviation of the sinusoidal shell modulation with an amplitude of 0.5 OD imaged by the system using Eqs. (2)–(7) without approximation and by using a linear approximation [Eq. (13)]. This calculated deviation is of the order of ~6%.

Conclusions

An imaging system based on the pinhole camera, framing camera, film, and digitization was characterized. This system has been used in spherical implosion experiments to measure shell integrity. Hot-core emission, which was used as a backlighter for the cold shell, was imaged at x-ray energies above and below the Ti *K* edge. The difference between the two images was related to perturbations in the cold, or absorbing, part of the shell. Based on the measured resolution and noise, a Wiener filter has been formulated that reduces noise, compensates for detector resolution, and facilitates measurement of shell nonuniformities.

ACKNOWLEDGMENT

This work was supported by the U.S. Department of Energy Office of Inertial Confinement Fusion under Cooperative Agreement No. DE-FC03-92SF19460, the University of Rochester, and the New York State Energy Research and Development Authority. The support of DOE does not constitute an endorsement by DOE of the views expressed in this article.

REFERENCES

1. D. K. Bradley, J. A. Delettrez, R. Epstein, R. P. J. Town, C. P. Verdon, B. Yaakobi, S. Regan, F. J. Marshall, T. R. Boehly, J. P. Knauer, D. D. Meyerhofer, V. A. Smalyuk, W. Seka, D. A. Haynes, Jr., M. Gunderson, G. Junkel, C. F. Hooper, Jr., P. M. Bell, T. J. Ognibene, and R. A. Lerche, Phys. Plasmas **5**, 1870 (1998).

2. B. Yaakobi, V. A. Smalyuk, J. A. Delettrez, R. P. J. Town, F. J. Marshall, V. Yu. Glebov, R. D. Petrasso, J. M. Soures, D. D. Meyerhofer, and W. Seka, in *Inertial Fusion Sciences and Applications 99*, edited by C. Labaune, W. J. Hogan, and K. A. Tanaka (Elsevier, Paris, 2000), pp. 115–121.

3. B. Yaakobi, V. A. Smalyuk, J. A. Delettrez, F. J. Marshall, D. D. Meyerhofer, and W. Seka, Phys. Plasmas **7**, 3727 (2000).

4. V. A. Smalyuk, B. Yaakobi, F. J. Marshall, and D. D. Meyerhofer, in *Atomic Processes in Plasmas: Twelfth Topical Conference*, edited by R. C. Mancini and R. A. Phaneuf (American Institute of Physics, New York, 2000), pp. 15–24.

5. T. R. Boehly, D. L. Brown, R. S. Craxton, R. L. Keck, J. P. Knauer, J. H. Kelly, T. J. Kessler, S. A. Kumpan, S. J. Loucks, S. A. Letzring, F. J. Marshall, R. L. McCrory, S. F. B. Morse, W. Seka, J. M. Soures, and C. P. Verdon, Opt. Commun. **133**, 495 (1997).

6. Y. Lin, T. J. Kessler, and G. N. Lawrence, Opt. Lett. **20**, 764 (1995).

7. S. Skupsky, R. W. Short, T. Kessler, R. S. Craxton, S. Letzring, and J. M. Soures, J. Appl. Phys. **66**, 3456 (1989).

8. D. K. Bradley, P. M. Bell, O. L. Landen, J. D. Kilkenny, and J. Oertel, Rev. Sci. Instrum. **66**, 716 (1995).

9. G. O. Reynolds *et al.*, *The New Physical Optics Notebook: Tutorials in Fourier Optics* (SPIE Optical Engineering Press, Bellingham, WA, 1989).

10. R. E. Turner *et al.*, "Comparison of CCD versus Film Readouts for Gated MCP Cameras," to be published in the Review of Scientific Instruments.

11. H. F. Robey, K. S. Budil, and B. A. Remington, Rev. Sci. Instrum. **68**, 792 (1997).

12. V. A. Smalyuk, T. R. Boehly, D. K. Bradley, J. P. Knauer, and D. D. Meyerhofer, Rev. Sci. Instrum. **70**, 647 (1999).

13. J. D. Wiedwald *et al.*, in *Ultrahigh- and High-Speed Photography, Videography, Photonics, and Velocimetry '90*, edited by L. L. Shaw, P. A. Jaanimagi, and B. T. Neyer (SPIE, Bellingham, WA, 1990), Vol. 1346, pp. 449–455.

14. W. H. Press *et al.*, *Numerical Recipes in FORTRAN: The Art of Scientific Computing*, 2nd ed. (Cambridge University Press, Cambridge, England, 1992), pp. 701–715.